





Atomic-scale manipulation of buried graphene–silicon carbide interface by local electric field

Marek Kolmer ^{1✉}, Joseph Hall^{1,2}, Shen Chen ¹, Samuel Roberts², Zhe Fei ^{1,2}, Yong Han ^{1,2} & Michael C. Tringides^{1,2}

Precision of scanning tunneling microscopy (STM) enables control of matter at scales of single atoms. However, transition from atomic-scale manipulation strategies to practical devices encounters fundamental problems in protection of the designer structures formed atop the surface. In this context, STM manipulation of subsurface structures on technologically relevant materials is encouraging. Here, we propose a material platform and protocols for precise manipulation of a buried graphene interface. We show that an electric field from the STM tip reversibly controls breaking and restoring of covalent bonds between the graphene buffer layer and the SiC substrate. The process involves charge redistribution at the atomically sharp interface plane under the epitaxial graphene layer(s). This buried manipulation platform is laterally defined by unit cells from the corresponding $(6\times 6)_{\text{SiC}}$ moiré lattice of the epitaxial graphene. Local and reversible electric-field-induced patterning of graphene heterostructures from the bottom interface creates an alternative architecture concept for their applications.

¹Ames National Laboratory, U.S. Department of Energy, Ames, IA 50011, USA. ²Department of Physics and Astronomy, Iowa State University, Ames, IA 50011, USA. ✉email: mkolmer@ameslab.gov

Since the controlled positioning of 35 single Xe adatoms on a single crystal Ni(110) surface in the work by Eigler and collaborators¹, scanning tunneling microscopy (STM) has been considered not only an imaging and spectroscopic technique but also as a unique instrument capable of fabricating designer structures at the atomic scale^{2,3}. Over the years, STM manipulation of surface adsorbates^{4–10} and surface atom vacancies^{11–13} has progressed from both technical and conceptual points of view (Fig. 1a). Particularly, the design of specific systems facilitating reliable STM operation has shown the fabrication of unprecedentedly complex structures through thousands of controlled manipulation events. For example, carbon monoxide molecules adsorbed on Cu(111) at cryogenic temperatures were arranged in hierarchies performing basic logic operations⁵ or in artificial lattices expressing highly tunable electronic bands^{8,14,15}. Even higher stability of surface vacancies in the Cl layer on Cu(110) enabled the atom-by-atom realization of a one-kilobyte

memory¹², establishing state-of-the-art status for STM manipulations.

However, the transfer of such accomplishments from metal substrates to more application-relevant systems is challenging. It requires a careful combination of STM manipulation protocols with material design, synthesis, and processing. Hydrogenated Si(100)^{11,13} is one of the most successful examples, where Simmons and collaborators used STM-stimulated desorption of single H atoms to fabricate devices realizing single-atom transistors¹⁶ or coupled qubits¹⁷. For these applications, the synthesis and processing steps are indeed critical, as STM lithographic patterns form the only chemically active sites for phosphine molecule adsorption, from which phosphorous dopants are subsequently incorporated into the crystalline lattice, thermally activated, and finally protected by a few layers of post-deposited Si.

The larger band-gap semiconductor, silicon carbide (SiC), constitutes another technologically important material with

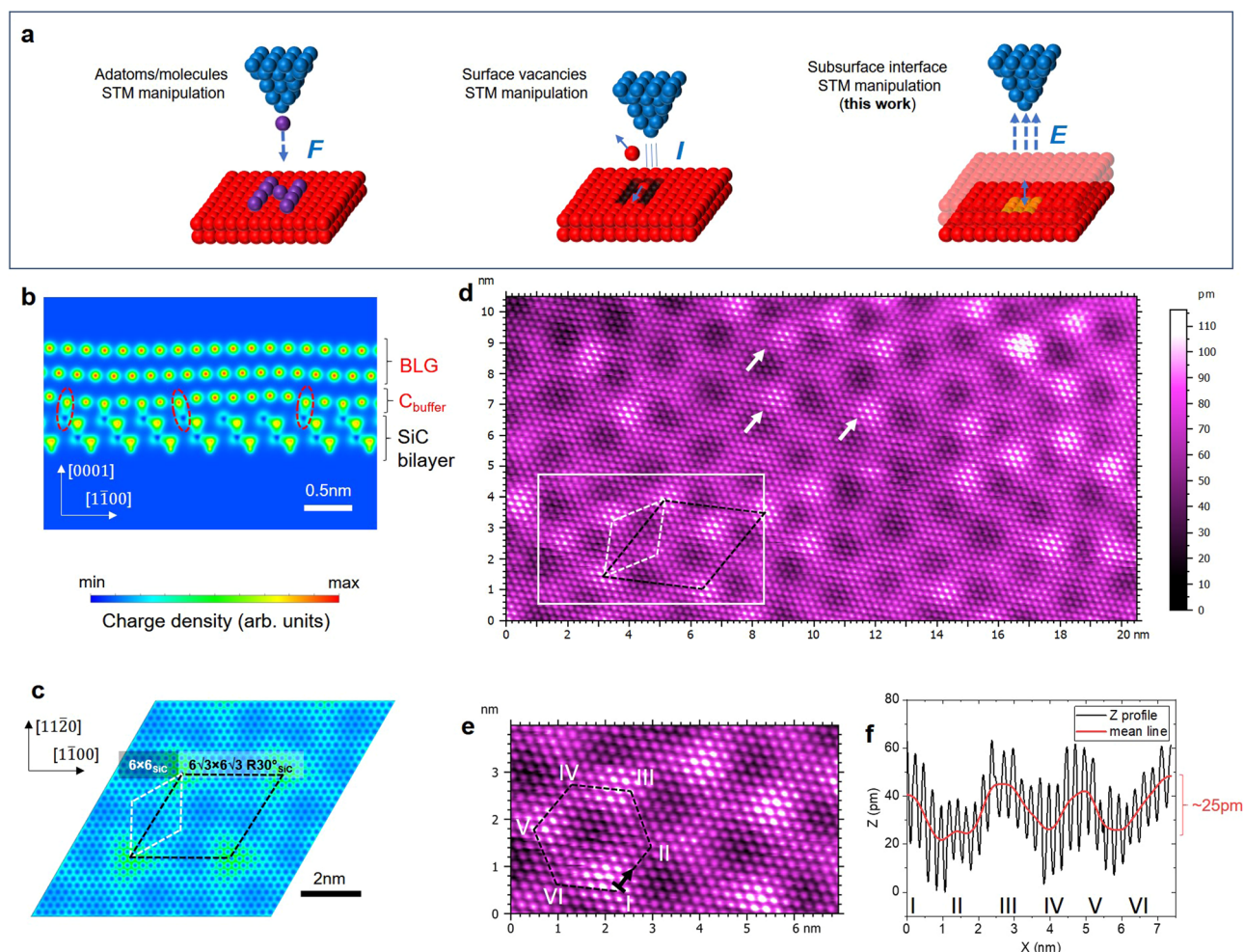


Fig. 1 Buried interface under epitaxial bilayer graphene on SiC(0001). **a** Schematics of scanning tunneling microscopy (STM)-based manipulation procedures and corresponding physical mechanism involved (F : force; I : inelastic tunneling; E : electric field)^{2,3}. In the cases of surface atoms and adsorbates, the surface atomic layer gives the manipulation plane, where the corresponding surface reconstructions define the in-plane manipulation sites. This work introduces material and experimental protocols for an analogous manipulation platform consisting of covalent Si-C bonds at the atomically sharp, buried interface. **b** Calculated charge density distribution across the regular interface of epitaxial bilayer graphene (BLG) and SiC substrate. AB-stacked BLG on top is decoupled from SiC by the graphene buffer layer (C_{buffer}). Red dashed ellipses mark examples of covalent sp^3 bonds (shared charge density) between C_{buffer} and interface Si atoms. **c** Calculated charge density distribution at ~ 0.1 nm above BLG atoms along (0001)_{SiC} plane. Black and white dashed rhombuses mark two corresponding SiC unit cells, which are the same size as in **d**. The color bar is the same in **b**, **c**. **d**, **e** STM constant-current topographies (sample bias, $U = -10$ mV, and tunneling current, $I = 500$ pA). Note that low-bias STM topography of AB-stacked BLG exhibits atomic contrast of only one sublattice from the top layer⁷⁰. White arrows mark examples of protrusions on the regular, quasi-hexagonal moiré interface structure. The area marked by a white line rectangle is presented in **e**. **f** Cross-section along the hexagonal path marked in panel **e**. Atomic-contrast corrugation (black line) is removed by a low-pass Gaussian filter (red line).

applications varying from high-power microelectronics¹⁸ to quantum information processing^{19,20}. Controlled thermal decomposition of the top SiC layers also allows for precise growth of epitaxial graphene-SiC heterostructures^{21–26}. Due to their high mesoscale quality and compatibility of the SiC(0001) substrate with general semiconductor processing strategies, these epitaxial graphene-based systems attract significant attention^{27–31}. In this case, the interface between the first epitaxial graphene layer (buffer layer; C_{buffer}) and SiC are primarily responsible for their unique electronic properties^{32–35}. Controlling over this interface tunes the graphene electronic states, which leads to a rich variety of systems manifesting graphene-based physics of fundamental interest. Particularly, they include ballistic transport in topological edge states of graphene nanoribbons^{28,29,31,36}, graphene flat bands^{34,35}, strain-induced pseudo-magnetic fields³⁰, or superconductivity via intercalation of the interface^{37–40}. On the other hand, epitaxial graphene is routinely used as a model material system, e.g., to study electric-field-dependent single-atom chemical bonding between metal and graphene⁴¹, or structural dislocations of graphene⁴² and their dynamics⁴³. Finally, improved synthesis methods of a high-quality, long-range ordered interface between C_{buffer} and SiC have recently enabled semiconducting graphene, a long-standing challenge^{44–46}.

In epitaxial graphene, C_{buffer} consists of sp^2 hybridized C atoms arranged in quasi-hexagonal $(6 \times 6)_{\text{SiC}}$ moiré pattern. This graphene-like network is separated by sp^3 hybridized C atoms covalently bonded to Si from the substrate. It was also shown that C_{buffer} and the underlying top SiC layer form incommensurate lattices⁴⁵, slightly deviating from the $(6\sqrt{3} \times 6\sqrt{3})R30^\circ_{\text{SiC}}$ reconstruction model⁴⁷. The resulting local stress additionally modulates the interface structure by producing larger patches of decoupled graphene. Importantly, the breaking of covalent bonds between C_{buffer} and SiC is associated with charge redistribution across the interface, as shown globally by rapid cooling synthesis²⁵ or hydrogenation^{48,49}.

Here, we use the above properties of the epitaxial graphene to design a platform for STM manipulation of bilayer graphene (BLG) and monolayer graphene (MLG) heterostructures on the SiC(0001) substrate. We show that the inherent local stress from the incommensurate lattices forming the C_{buffer} -SiC interface under the epitaxial graphene creates a fine balance for local covalent coupling of C_{buffer} to the SiC substrate; which consequently could be reversibly controlled by the application of an electric field with the use of STM setup. The charge separation resulting from covalent bonds' redistribution is used to pull or push the interface atoms depending on the polarity of the tip-sample bias voltage. The reported effect allows us to pattern the otherwise chemically inert epitaxial graphene with remarkable lateral precision, reaching single unit cells of the interface moiré lattice (~ 1.8 nm). Similar electric-field-induced manipulation procedures for graphene heterostructures on hexagonal boron nitride (hBN) have provided highly tunable control over graphene local doping levels at the nanometer-scale^{50–53}. Moreover, subsurface atom manipulations with STM electric field have also been achieved in other semiconducting systems like GaAs^{54–57}, ZnO⁵⁸, or PdSe₂⁵⁹ by redistribution of single charged defects (dopants or vacancies). However, in contrast to these investigations, our system provides a more defined subsurface STM manipulation landscape by synthesizing a buried two-dimensional interface expressing ferroelectric-like switching behavior⁶⁰.

Results

The interface of the graphene buffer layer and SiC. Figure 1b displays a cross-section of the epitaxial BLG interface in the form

of a charge density map modeled by our density functional theory (DFT) calculations (see Methods for details). It consists of three layers of C atoms atop a SiC bilayer. The top two layers of purely sp^2 hybridized C form the AB-stacked BLG. In contrast, the hybrid third layer (C_{buffer}) possesses some sp^3 hybridized atoms, which are covalently bonded to the underlying Si as manifested by the shared charge densities (red ellipses). The C_{buffer} and SiC lattices are rotated by 30° creating a complex moiré pattern of these covalent bonds, and thus the effective corrugation of the whole BLG heterostructure exhibits a faint, quasi-hexagonal $(6 \times 6)_{\text{SiC}}$ periodicity (Fig. 1c). The proposed $(6\sqrt{3} \times 6\sqrt{3})R30^\circ_{\text{SiC}}$ and $(13 \times 13)C_{\text{buffer}}$ supercell, which is used in our calculations, still includes a small tensile strain ($\sim 0.4\%$)⁶¹ in comparison to the unit cell of free-standing graphene. As a result, part of the quasi-hexagonal moiré pattern in the relaxed DFT structure is more protruded (green color in Fig. 1c) due to the breaking of additional covalent bonds between C_{buffer} and SiC (Supplementary Fig. 1).

The above model corresponds well to our low-bias STM topography of the ultra-high vacuum synthesized epitaxial BLG (for synthesis details see Methods and ref. 62) presented in Fig. 1d (all STM experiments were performed at ~ 78 K). Positions of the protruded parts of the BLG interface, exemplified by the white arrows, are spanned by the $(6 \times 6)_{\text{SiC}}$ lattice unit vectors. They may occupy any of the three alternating corners of the quasi-hexagonal pattern (Fig. 1e). Cross-section of the high-resolution STM in Fig. 1f shows that these protrusions extend only about 25 pm from the regular moiré corrugation. This small value supports the findings of our DFT and points to the local changes of covalent coupling within the buried interface between C_{buffer} and SiC as a natural origin of the observed protrusions⁶³. Moreover, due to the difference in thermal expansion coefficients of graphene and SiC²⁵, the covalent coupling between C_{buffer} and SiC should depend on kinetic conditions during synthesis. In this work, extended annealing times at the SiC graphitization step (1 h at ~ 1570 K for BLG and 1 h at ~ 1470 K for MLG) followed by progressive two-step cooling under ultra-high vacuum resulted in protrusion surface densities of about 0.4 per one $(6 \times 6)_{\text{SiC}}$ unit cell [~ 1.2 per $(6\sqrt{3} \times 6\sqrt{3})R30^\circ_{\text{SiC}}$], matching the DFT model predictions.

Evidence of electric-field-induced interface manipulation.

Interestingly, stable configurations of the moiré pattern protrusions change upon STM imaging performed with larger bias voltages, as seen in Fig. 2a under the atomically resolved top BLG lattice. The observed dynamic behavior depends on the polarity of the applied voltage. Particularly, large negative sample biases decrease the average number of protrusions, while large positive biases increase it (Fig. 2b). This manipulation process is reversible. Additionally, imaging at low sample biases and tunneling currents (soft STM scanning conditions) exhibits hysteresis effects depending on the previously used conditions, so the density of the protrusions can be controlled (Supplementary Fig. 2). These results particularly exclude the origination of these features from heteroatoms, i.e., Si, consistent with former studies showing a chemically homogenous interface⁶⁴.

Figure 2c presents a quantitative analysis of the protrusion density as a function of STM sample bias voltage for a given area of BLG/SiC and tunneling current. The experiment consisted of two datasets of STM images obtained for sequentially increasing negative and positive sample bias voltages (Supplementary Fig. 3). Before collecting each set, the area was imaged with a large negative voltage, which, due to the hysteresis effect, resulted in low starting surface densities of protrusions [$\sim 0.2/(6 \times 6)_{\text{SiC}}$]. For the negative sample biases, the number of protrusions initially increases up to the level close to native surface densities [$\sim 0.4/$

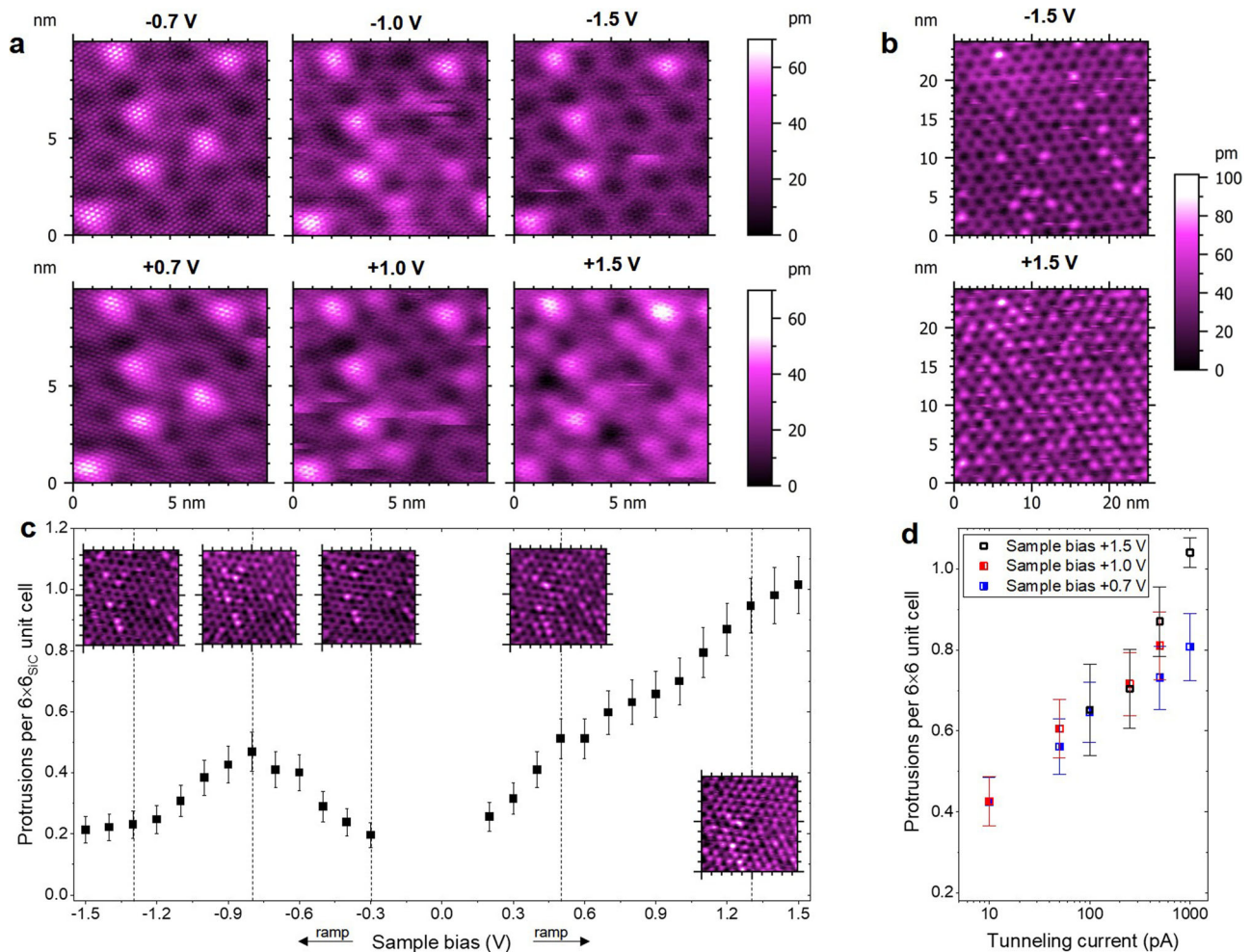


Fig. 2 Evolution of bilayer graphene-SiC interface during scanning tunneling microscopy (STM) experiments. **a, b** STM constant-current ($I = 100$ pA) topographies of two surface regions (**a** $10\text{ nm} \times 10\text{ nm}$ and **b** $25\text{ nm} \times 25\text{ nm}$) obtained for larger sample biases as indicated above each panel. **c** Surface densities of the protrusions as a function of STM sample bias ($I = 500$ pA). The data set was obtained in the same surface region. Due to hysteresis effects, the area was imaged with negative sample bias ($U = -1.5\text{ V}$, $I = 500$ pA) before starting each voltage ramp (arrows). Insets present representative STM images ($20\text{ nm} \times 20\text{ nm}$). **d** Surface densities of the protrusions as a function of STM current for three different positive sample biases. The experiments were not performed in the same surface regions. Note the logarithmic scale of the tunneling current. Error bars in **c** and **d** represent standard error calculated assuming a Poisson distribution of protrusions.

$(6 \times 6)_{\text{SiC}}$], and then progressively decreases to the initial, low value. In contrast, for the positive voltages, we observe a monotonic, close to linear, increase in surface densities up to the level reaching about one protrusion per $(6 \times 6)_{\text{SiC}}$ unit cell. For the positive voltages, the density also increases linearly with the logarithm of the tunneling current (Fig. 2d). Such a weak tunneling current dependence, together with the above bias voltage polarity dependences, point to the STM-induced, local electric field^{50,59,65,66} as a source of the manipulation.

Small effective electric fields during soft STM scanning conditions, e.g., $|U| < 0.4\text{ V}$ and $I < 100$ pA, do not modify metastable configurations of the interface protrusions, i.e., for densities close to equilibrium (but high-density phases are stabilized by large positive voltages). This fact enables nanometer-scale STM patterning of BLG/SiC heterostructure, as exemplified in Supplementary Fig. 4, where a manipulation protocol involving large bias constant-current imaging increases the surface density of protrusions.

The experiments performed on MLG/SiC show that the densities of the observed protrusions also depend on the bias voltage used for STM imaging (Supplementary Fig. 5a–c). As in the BLG case, soft STM imaging conditions preserve different

metastable configurations of protrusions. Consequently, we also performed nanometer-scale patterning of MLG using large bias constant-current STM conditions (Supplementary Fig. 5d, f). Quantitative agreement in the results for MLG and BLG independently supports the buried interface modification as the origin of manipulation.

Downscaling of STM manipulation to single moiré sites.

Observation of metastable configurations of protrusions under soft STM scanning conditions could be further used to scale down our manipulation protocols to reach lateral precision of a single moiré $(6 \times 6)_{\text{SiC}}$ lattice site. In this case, we stabilize the position of the STM tip above a certain corner of the moiré pattern on BLG/SiC (Fig. 3a). Then, to create a protrusion under constant-height STM operation conditions, we initialized a positive sample bias voltage ramp loop (Fig. 3b). An abrupt rise of the tunneling current signal, followed by a clear hysteresis, manifests the formation of a protrusion underneath (due to decrease of distance between the tip and the top graphene layer). This is proven by a subsequent STM scan (Fig. 3a, middle panel). This manipulation process is not only reversible, as shown by a similar procedure

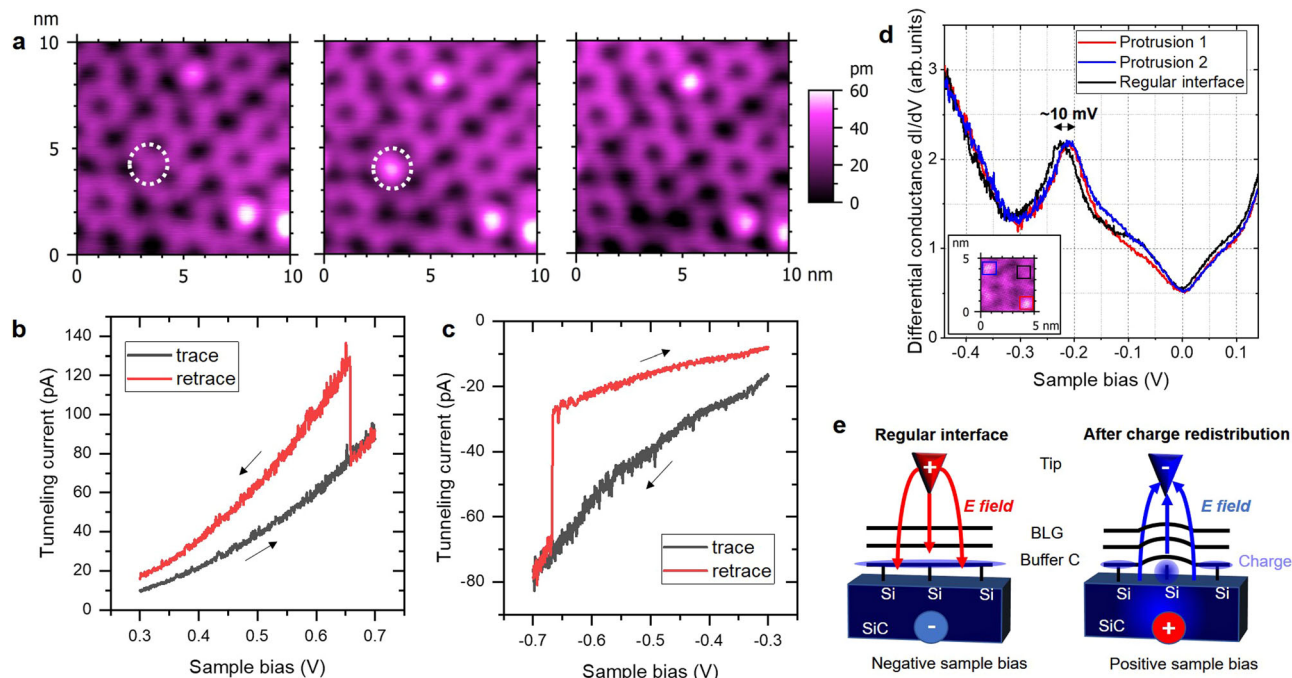


Fig. 3 Reversible, single-site interface manipulation by local scanning tunneling microscopy (STM) electric field. **a** Sequence of three consecutive STM constant-current ($U = +0.3$ V, $I = 25$ pA, 10 nm \times 10 nm) topographies of the same surface region of the epitaxial bilayer graphene (BLG) heterostructure. Due to soft scanning conditions, an atomic contrast of top BLG is not registered. The white, dashed circles mark lateral positions of the STM tip during constant-height (STM feedback loop is open) sample bias voltage ramps. **b** Tunneling current signal registered during positive voltage ramp loop (see arrows). Vertical tip-sample distance is defined by $U_0 = +0.3$ V and $I_0 = 10$ pA. The total temporal scale of the ramp loop $t = 2048$ ms. The rapid increase in signal relates to the creation of a single protrusion underneath the STM tip. **c** Tunneling current signal registered during negative voltage ramp loop ($U_0 = -0.3$ V, $I_0 = 20$ pA, $t = 2048$ ms). Rapid decrease in the absolute value of current relates to the annihilation of a single protrusion underneath the STM tip. Note the negative sign of tunneling current. **d** Local variation of scanning tunneling spectroscopy differential conductance $dI/dV(U)$ data (constant-height, $U_0 = -0.45$ V, $I_0 = 300$ pA). Corresponding spectra are collected at corners of the moiré pattern hosting a regular interface (black) and two protrusions (red and blue). Each spectrum is averaged over 49 (7×7) single curves spanning the square regions marked on the inset STM topography. Note that the limited range of voltages and tunneling currents used for $dI/dV(U)$ spectroscopy did not modify the interface structure. **e** Schematic presenting a manipulation mechanism based on the charge redistribution across the interface of the graphene buffer layer and SiC for two different voltage polarities.

performed for negative voltage (Fig. 3c), but also highly reproducible (Supplementary Fig. 6 and Supplementary Movies 1–3). It allows local control of the protrusion arrangement, forming predefined structures. However, often, a single voltage ramp creates or annihilates additional protrusions in the vicinity of the targeted location. Nevertheless, as the process is easily reversible, a series of consecutive manipulations could create an intended pattern. The same manipulation strategy applies to the MLG/SiC system (Supplementary Fig. 7 and the corresponding Supplementary Movie 4).

To determine the influence of the interface protrusions on the electronic properties of BLG, we also performed a scanning tunneling spectroscopy experiment (Fig. 3d). Differential conductance dI/dV spectra obtained above the corners of the moiré interface pattern match closely to the former STM reports of epitaxial BLG on SiC(0001)^{62,67–70}, particularly featuring a n-doped BLG system with a Dirac point located about 0.33 eV below the Fermi level. Comparison between spectra above protrusions and a regular interface shows consistent shift of about 10 mV towards positive voltages for the dI/dV spectra of protrusions. Due to efficient screening by the large density of electronic states from the top BLG layers, such small changes are expected^{50,69}. The shift of spectra towards a neutral graphene electronic configuration directly above the protrusions supports the mechanism of electric-field-induced charge redistribution at the interface, which accompanies the detachment of C_{buffer} from the SiC substrate (Fig. 3e). This interpretation is also consistent

with the photoelectron spectroscopy experiments performed after global decoupling of epitaxial graphene^{25,48}, presenting the same trend of p-doping towards a neutral, freestanding system.

Interface structural changes upon manipulation from DFT.

Our DFT calculations performed for the $6\sqrt{3}a_{\text{SiC}} \times 6\sqrt{3}a_{\text{SiC}}$ slab of BLG on SiC(0001) found degenerate configurations with a single protrusion, whose position depends on the initial configuration of atoms. Figure 4 depicts the results from such two configurations, A and B, for each of which the protrusion position is separated by a distance of about $(6 \times 6)_{\text{SiC}}$, matching the experimental findings about their possible locations. These configurations mimic the transition between two metastable states upon STM manipulation. A comparison of the calculated charge densities across the interface plane shows a change in covalent coupling between C_{buffer} and terminal Si atoms associated with annihilation or formation of the protrusion (Fig. 4a, b and Fig. 4e, f, respectively). Figure 4c, g presents the exact C-Si covalent bond distributions at the interface in the form of charge density difference (CDD) maps. Here, CDD is defined as $\Delta\rho = \rho_{\text{GSiC}} - \rho_{\text{G}} - \rho_{\text{SiC}}$, where ρ_{GSiC} , ρ_{G} and ρ_{SiC} are charge densities of whole BLG-SiC slab, freestanding trilayer graphene slab, and freestanding Si-terminated SiC(0001) slab, respectively. Our model shows that the annihilation or formation of a single protrusion affects several C-Si bonds at the interface, i.e., the annihilation of the protrusion region presented in the top

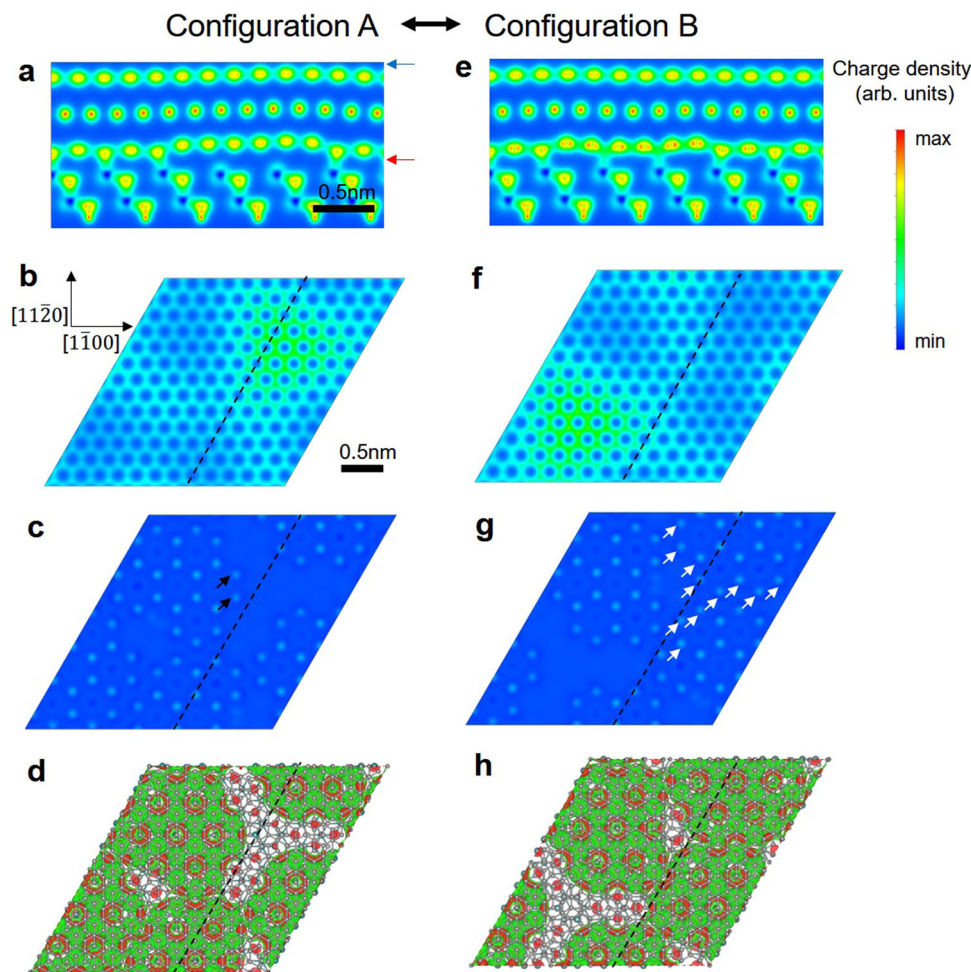


Fig. 4 Redistribution of C-Si covalent bonds and charge upon switching of a protrusion site. **a** Calculated charge density distribution across a regular interface of the epitaxial bilayer graphene (BLG) in configuration A along the protrusion location as marked by the dashed lines in panels **b-d**. **b** Calculated charge density distribution of the $6\sqrt{3}a_{\text{SiC}} \times 6\sqrt{3}a_{\text{SiC}}$ supercell at -0.1 nm above BLG top atoms along $(0001)_{\text{SiC}}$ plane as indicated by the blue arrow in **a**. **c** Calculated charge density difference (CDD) at the interface plane as indicated by the red arrow in **a**. The bright features in **c** (larger CDD values) correspond to C-Si covalent bonds (see Supplementary Fig. 1d for the exact locations of atoms). **d** Charge accumulation (red) and depletion (green) at the interface are displayed as a top view of the corresponding CDD isosurfaces with a magnitude of $0.002 e \text{ bohr}^{-3}$ (arbitrarily chosen to present data in three-dimensional space). For a perspective view see Supplementary Fig. 8. **e-h** Same as **a-d** but for BLG/SiC in configuration B. The C-Si bonds affected by the manipulation of the upper right protrusion are indicated by two black arrows in **c** and eleven white arrows in **g**. The color scale for **a-c** and **e-g** is the same.

right part in Fig. 4g creates eleven new C-Si covalent bonds, while two previously present bonds in Fig. 4c are broken. As the change of sp^2 hybridization of the C_{buffer} atoms into sp^3 increases the bond lengths within the graphene buffer layer (sp^3 bonds are longer than sp^2), this complex behavior is associated with the release of a tensile strain created upon the formation of new C-Si covalent bonds^{45,71}.

Moreover, the CDD isosurfaces presented in Fig. 4d, h help to visualize a charge redistribution upon formation or annihilation of a protrusion site. Due to the lack of C-Si covalent bonds, there is minimal charge transfer between SiC and C_{buffer} directly below the protrusion site around the area of ~ 0.75 nm in diameter (see also Supplementary Fig. 8). In contrast, in the same region without the protrusion, when C_{buffer} is covalently coupled to SiC, the charge transfer from SiC to C_{buffer} occurs³⁴. These results rationalize the mechanism presented schematically in Fig. 3e.

Local STM tip position dependence. Finally, we investigated a detailed position dependence of our local manipulation protocol for the formation of protrusions on the BLG/SiC system (Fig. 5a).

To probe different lateral locations of the moiré corrugation pattern, we set a series of positive sample bias voltage ramps over a grid consisting of 86×86 points spanning an area of $10 \times 10 \text{ nm}^2$. First, from the fragmented STM image collected during the experiment (Fig. 5b), we obtain a distribution of the metastable protrusion locations. It is important to note that since soft imaging conditions were used in between positive voltage ramps, the local structure is not stabilized by the STM-induced electric field. The protrusions closely follow the $(6 \times 6)_{\text{SiC}}$ lattice, but the corresponding sites are not equivalent. Moreover, the interplay between local stress within the heterostructure precludes the formation of a complete lattice, i.e., the formation of a dense protrusion pattern in one part, annihilates them in the other. This effect is clearly seen via analysis of the single voltage ramp spectra performed away from the $(6 \times 6)_{\text{SiC}}$ lattice sites. In this case, as the tip is in between two or three switchable interface locations, we often observe multiple switching events caused by inherent instabilities (Fig. 5c). In contrast, for locations directly above protrusions, we generally do not register any switching events, because once a protrusion is formed, it is stable under positive voltage conditions.

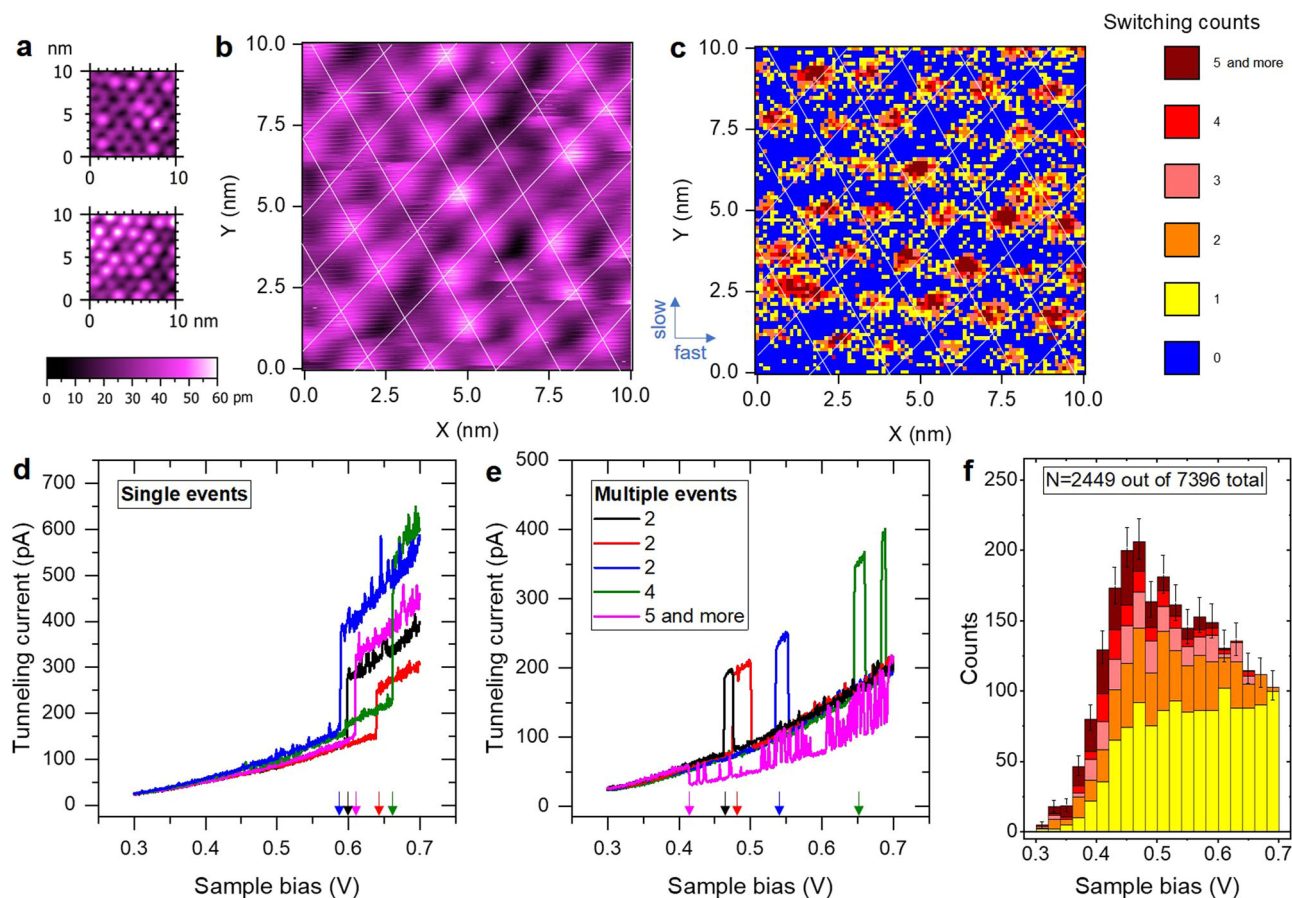


Fig. 5 Tip position dependence for local scanning tunneling microscopy (STM) manipulations. **a** STM constant-current topographies ($U = +0.3$ V, $I = 25$ pA) of the same surface region of the epitaxial bilayer graphene obtained before and after a position-dependent manipulation experiment. **b** STM constant-current topography ($U = +0.3$ V, $I = 25$ pA) obtained during a position-dependent manipulation experiment. The image is built from 86 fragmented vertical datasets registered after each line of 86 single-point I - V dependences collected along the fast scan direction (see the blue arrows). **c** Two-dimensional map showing the distribution of protrusion switching counts obtained from a grid of 86 by 86 point I - V dependences for positive sample bias voltage ramps from $+0.3$ V to $+0.7$ V (constant-height is defined at each point from $U_0 = +0.3$ V, $I_0 = 25$ pA, temporal scale of one ramp $t = 1024$ ms). A single count is defined as a rapid increase or decrease of the tunneling current signal ($>15\%$ of its previous value). The thin white lines in **b** and **c** are $(6 \times 6)_{\text{SiC}}$ grids guiding the eye for positions of the moiré pattern exhibiting protrusions. **d, e** Examples of single I - V curves from the experiment showing single (**d**) and multiple (**e**) switching events. Arrows point to the lowest threshold voltages that induce switching. **f** Histogram presenting the distribution of switching threshold voltages. Colors are associated with corresponding switching counts in panel **c**.

Figure 5d, e presents examples of single-point spectra from the experiment for single and multiple switching events, respectively. The single events dominate (apart from zero events), they generally exhibit larger changes in tunneling current signals and larger threshold voltages (Fig. 5f). This behavior is caused mainly by the lateral distribution of single switching events close to the locations of expected protrusions. These results clarify the reproducibility of the previously described manipulation protocol by presenting its limitations, which are particularly strongly related to the position of the STM tip with respect to the $(6 \times 6)_{\text{SiC}}$ moiré lattice. On the other hand, the reversibility of the processes opens a possibility for the implantation of autonomous STM patterning procedures and their further optimization.

Conclusions

In summary, we have developed an ultimately precise buried manipulation platform for model two-dimensional heterostructures: epitaxial bilayer and monolayer graphene grown on SiC(0001). It consists of an atomically sharp moiré interface underneath the top graphene layer(s). We have shown that the application of an electric field from the scanning tunneling microscope controls the attachment of the underlying buffer layer

to the SiC substrate in locations laterally defined by their $(6 \times 6)_{\text{SiC}}$ moiré lattice vectors, resulting in the formation of defined and metastable patterns of protrusions on the epitaxial graphene heterostructures. We have quantitatively investigated the corresponding STM manipulation conditions on the epitaxial bilayer graphene, while the epitaxial monolayer graphene qualitatively has shown the same behavior. Our DFT modeling explains that this highly reversible and local ferroelectric-like switching is due to the charge redistribution associated with breaking and restoring the corresponding C-Si covalent bonds. The intrinsic, tensile interface strain enhances this process.

The results present an architecture for local patterning of epitaxial graphene heterostructures with the precision of single $(6 \times 6)_{\text{SiC}}$ moiré lattice vectors (see Fig. 6a). Due to the complex electric-field-related mechanism and the interplay between structural stress at the interface, in the formation of designer structures, this lateral precision must be accompanied with limitations in their local densities. However, for densities close to the thermodynamic equilibrium, the protrusions could be locally arranged in ordered superstructures (Fig. 6b, c). This opens perspectives for locally tunable graphene superstructures formed directly within the epitaxial graphene systems. In contrast to

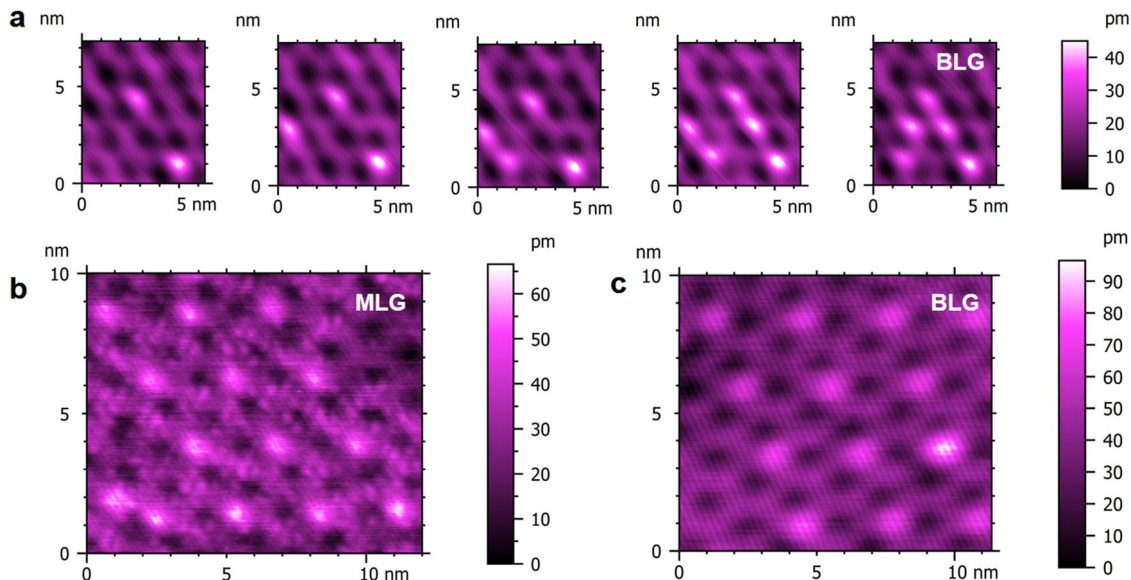


Fig. 6 Buried interface manipulation perspectives. **a** Series of scanning tunneling microscopy (STM) constant-current topographies ($U = +0.5$ V, $I = 100$ pA) presenting the formation of closely packed protrusions on the epitaxial bilayer graphene (BLG), forming the “A” pattern from the $(6 \times 6)_{\text{SiC}}$ moiré lattice sites. **b, c** STM constant-current topographies ($U = +0.3$ V, $I = 25$ pA) presenting examples of 12 protrusions forming the (3×4) lattice of the $(13 \times 13)_{\text{C}_{\text{buffer}}}$ supercells on the epitaxial monolayer graphene (MLG, **b**) and BLG (**c**), respectively. Note specific interface electronic states contrast in the STM topography of MLG in **b**, similar to previous reports^{41,68,80}.

STM-based manipulation platforms on metallic^{4,5,8,12,14,15} or semiconducting¹⁰ substrates, the inherent graphene Dirac electrons and low density of states from the silicon carbide create an opportunity for exploring rich quantum phases in low-energy electronic excitations of tailored graphene superlattice minibands^{72–74}.

Methods

Synthesis. The epitaxial monolayer graphene (MLG) and bilayer graphene (BLG) synthesis for the majority of the work was performed at the Ames National Laboratory in two custom-made ultra-high vacuum systems with base pressures below 1×10^{-10} mbar. Our 6H-SiC(0001) substrates (n-type, 330 μm , 0.02–0.2 $\Omega\cdot\text{cm}$) were purchased from University Wafers Inc or Cree Inc and diced into 9 mm \times 1.5 mm samples. After an introduction to ultra-high vacuum, samples were outgassed for several hours at temperatures up to ~ 870 K. Epitaxially grown MLG/BLG on Si-face were synthesized by thermal annealing for 1 h at ~ 1470 K and ~ 1570 K, respectively. The temperature was monitored by an infrared pyrometer. During annealing, the pressure in the chamber was kept below 3×10^{-10} mbar. Annealing was performed by direct current heating followed by a two-step cooling process. At first, samples were cooled down to room temperature by slow thermalization on a sample stage, followed by their introduction to a cryostat hosting a scanning tunneling microscope (STM) operating at liquid nitrogen temperature. To confirm the generality of the results, we reproduced the main findings of the work on a high-quality BLG/SiC(0001) heterostructure synthesized by BeeGraphene via Si beam-assisted graphitization of SiC^{24,26}. In this case, the external samples were shipped to the Ames National Laboratory, outgassed for several hours at ~ 570 K under ultra-high vacuum, and subsequently introduced to STM cryostat for characterization.

STM experiments. All STM experiments were performed at the Ames National Laboratory under liquid nitrogen conditions (~ 78 K) in the commercial Scienta-Omicron low-temperature STM. Tungsten STM tips were obtained by electrochemical

etching of W wire (99.95%, 0.25 mm) in NaOH solution. Before experiments, the tips were in situ prepared and tested on the Au(111) surface. Scanning tunneling spectroscopy data were collected with an external lock-in amplifier (MFLI, Zurich Instruments) with a frequency of 691 Hz and $V_{\text{AC}} = 15$ mV. Data from the externally prepared samples are presented in Supplementary Fig. 2 and Supplementary Fig. 3c, d (Sample type B).

DFT calculations. The first-principles calculations were performed based on density functional theory (DFT). We use the VASP code⁷⁵ with PAW pseudopotentials⁷⁶ and the optB88-vdW functional⁷⁷. The supercell $13a_G^* \times 13a_G^*$ matches $6\sqrt{3}a_{\text{SiC}} \times 6\sqrt{3}a_{\text{SiC}}$ (see Supplementary Fig. 1), where the lattice constant of 6H-SiC is $a_{\text{SiC}} = 3.09545$ Å and the lattice constant of top graphene is $a_G^* = \sqrt{3}a_{\text{SiC}}/2 \approx 2.681$ Å⁶¹. Thus, the top graphene has a tiny tensile strain of 0.4% relative to the underlying SiC(0001) substrate by considering the pristine graphene or graphite lattice constant $a_G = 2.465$ Å⁶¹. During relaxation, the bottommost C single-atom-thick layer is fixed with the dangling bonds passivated by pseudo-H atoms. The k mesh is taken to be $1 \times 1 \times 1$ due to the sufficiently large supercell size. The vacuum thickness along the direction perpendicular to the slab surface is 2 nm. The energy cutoff is set to be 550 eV. Spin polarization and dipole corrections are always considered, while spin-orbit coupling is not considered in this work⁷⁸. The force convergence tolerance is set to be no greater than 0.005 eV/Å. In the calculation for configuration A, we initially chose a slab with all atomic planes being flat. To obtain configuration B, we relax an initial structure in which the top three graphene layers are arranged to be mirror-image symmetric to those in the fully relaxed configuration A. All charge density and CDD plots are generated by the VESTA program⁷⁹.

Data availability

The data needed to reproduce the Figs. 1–6, Supplementary Fig. 1–8, and Supplementary Movies 1–4 are available from the corresponding author upon request.

Code availability

The work does not include any code development. The Python code used for data analysis is available from the corresponding author upon request.

Received: 30 October 2023; Accepted: 22 December 2023;

Published online: 06 January 2024

References

- Eigler, D. M. & Schweizer, E. K. Positioning single atoms with a scanning tunnelling microscope. *Nature* **344**, 524–526 (1990).
- Khajetoorians, A. A., Wegner, D., Otte, A. F. & Swart, I. Creating designer quantum states of matter atom-by-atom. *Nat. Rev. Phys.* **1**, 703–715 (2019).
- Ko, W., Ma, C. X., Nguyen, G. D., Kolmer, M. & Li, A. P. Atomic-scale manipulation and in situ characterization with scanning tunneling microscopy. *Adv. Funct. Mater.* **29**, 24 (2019).
- Crommie, M. F., Lutz, C. P. & Eigler, D. M. Confinement of electrons to quantum corrals on a metal surface. *Science* **262**, 218–220 (1993).
- Heinrich, A., Lutz, C., Gupta, J. & Eigler, D. Molecule cascades. *Science* **298**, 1381–1387 (2002).
- Hla, S.-W., Braun, K.-F., Wassermann, B. & Rieder, K.-H. Controlled low-temperature molecular manipulation of sexiphenyl molecules on Ag(111) using scanning tunneling microscopy. *Phys. Rev. Lett.* **93**, <https://doi.org/10.1103/physrevlett.93.208302> (2004).
- Strosio, J. A. & Celotta, R. J. Controlling the dynamics of a single atom in lateral atom manipulation. *Science* **306**, 242–247 (2004).
- Gomes, K. K., Mar, W., Ko, W., Guinea, F. & Manoharan, H. C. Designer Dirac fermions and topological phases in molecular graphene. *Nature* **483**, 306–310 (2012).
- Civita, D. et al. Control of long-distance motion of single molecules on a surface. *Science* **370**, 957 (2020).
- Sierda, E. et al. Quantum simulator to emulate lower-dimensional molecular structure. *Science* **380**, 1048–1052 (2023).
- Lyding, J. W., Shen, T. C., Hubacek, J. S., Tucker, J. R. & Abeln, G. C. Nanoscale patterning and oxidation of H-passivated Si(100)-2×1 surfaces with an ultrahigh vacuum scanning tunneling microscope. *Appl. Phys. Lett.* **64**, 2010–2012 (1994).
- Kalff, F. E. et al. A kilobyte rewritable atomic memory. *Nat. Nanotechnol.* **11**, 926–929 (2016).
- Achal, R. et al. Lithography for robust and editable atomic-scale silicon devices and memories. *Nat. Commun.* **9**, <https://doi.org/10.1038/s41467-018-05171-y> (2018).
- Slot, M. R. et al. Experimental realization and characterization of an electronic Lieb lattice. *Nat. Phys.* **13**, 672–676 (2017).
- Kempkes, S. N. et al. Design and characterization of electrons in a fractal geometry. *Nat. Phys.* **15**, 127–131 (2019).
- Fuechsle, M. et al. A single-atom transistor. *Nat. Nanotechnol.* **7**, 242–246 (2012).
- He, Y. et al. A two-qubit gate between phosphorus donor electrons in silicon. *Nature* **571**, 371–375 (2019).
- She, X., Huang, A. Q., Lucia, O. & Ozpineci, B. Review of silicon carbide power devices and their applications. *IEEE Trans. Ind. Electron.* **64**, 8193–8205 (2017).
- Christle, D. J. et al. Isolated electron spins in silicon carbide with millisecond coherence times. *Nat. Mater.* **14**, 160–163 (2015).
- Anderson, C. P. et al. Electrical and optical control of single spins integrated in scalable semiconductor devices. *Science* **366**, 1225–1230 (2019).
- Berger, C. et al. Ultrathin epitaxial graphite: 2D electron gas properties and a route toward graphene-based nanoelectronics. *J. Phys. Chem. B* **108**, 19912–19916 (2004).
- Riedl, C., Starke, U., Bernhardt, J., Franke, M. & Heinz, K. Structural properties of the graphene-SiC(0001) interface as a key for the preparation of homogeneous large-terrace graphene surfaces. *Phys. Rev. B* **76**, <https://doi.org/10.1103/physrevb.76.245406> (2007).
- Hupalo, M., Conrad, E. H. & Tringides, M. C. Growth mechanism for epitaxial graphene on vicinal 6H-SiC(0001) surfaces: a scanning tunneling microscopy study. *Phys. Rev. B* **80**, <https://doi.org/10.1103/physrevb.80.041401> (2009).
- De Heer, W. A. et al. Large area and structured epitaxial graphene produced by confinement controlled sublimation of silicon carbide. *Proc. Natl Acad. Sci.* **108**, 16900–16905 (2011).
- Bao, J. et al. Synthesis of freestanding graphene on SiC by a rapid-cooling technique. *Phys. Rev. Lett.* **117**, <https://doi.org/10.1103/physrevlett.117.205501> (2016).
- Ciochoń, P., Marzec, M., Olszowska, N. & Kołodziej, J. Reversible graphitization of SiC: a route towards high-quality graphene on a minimally step bunched substrate. *Appl. Surf. Sci.* **528**, 146917 (2020).
- Berger, C. et al. Electronic confinement and coherence in patterned epitaxial graphene. *Science* **312**, 1191–1196 (2006).
- Baringhaus, J. et al. Exceptional ballistic transport in epitaxial graphene nanoribbons. *Nature* **506**, 349–354 (2014).
- Aprojanz, J. et al. Ballistic tracks in graphene nanoribbons. *Nat. Commun.* **9**, <https://doi.org/10.1038/s41467-018-06940-5> (2018).
- Nigge, P. et al. Room temperature strain-induced Landau levels in graphene on a wafer-scale platform. *Sci. Adv.* **5**, eaaw5593 (2019).
- Prudkovskiy, V. S. et al. An epitaxial graphene platform for zero-energy edge state nanoelectronics. *Nat. Commun.* **13**, <https://doi.org/10.1038/s41467-022-34369-4> (2022).
- Ohta, T., Bostwick, A., Seyller, T., Horn, K. & Rotenberg, E. Controlling the electronic structure of bilayer graphene. *Science* **313**, 951–954 (2006).
- Rutter, G. M. et al. Scattering and interference in epitaxial graphene. *Science* **317**, 219–222 (2007).
- Marchenko, D. et al. Extremely flat band in bilayer graphene. *Sci. Adv.* **4**, eaau0059 (2018).
- Lu, Q. et al. Dirac fermion cloning, moiré flat bands, and magic lattice constants in epitaxial monolayer graphene. *Adv. Mater.* **34**, 2200625 (2022).
- Miettinen, A. L. et al. Edge states and ballistic transport in zigzag graphene ribbons: The role of SiC polytypes. *Phys. Rev. B* **100**, 045425 (2019).
- Kanetani, K. et al. Ca intercalated bilayer graphene as a thinnest limit of superconducting C6Ca. *Proc. Natl Acad. Sci. USA* **109**, 19610–19613 (2012).
- Briggs, N. et al. Atomically thin half-van der Waals metals enabled by confinement heteroepitaxy. *Nat. Mater.* **19**, 637–643 (2020).
- Toyama, H. et al. Two-dimensional superconductivity of Ca-intercalated graphene on SiC: vital role of the interface between monolayer graphene and the substrate. *ACS Nano* **16**, 3582–3592 (2022).
- Li, C. et al. Proximity-induced superconductivity in epitaxial topological insulator/graphene/gallium heterostructures. *Nat. Mater.* <https://doi.org/10.1038/s41563-023-01478-4> (2023).
- Omidian, M., Leitherer, S., Néel, N., Brandbyge, M. & Kröger, J. Electric-field control of a single-atom polar bond. *Phys. Rev. Lett.* **126**, 216801 (2021).
- Butz, B. et al. Dislocations in bilayer graphene. *Nature* **505**, 533–537 (2014).
- Endo, Y. et al. Dynamic topological domain walls driven by lithium intercalation in graphene. *Nat. Nanotechnol.* <https://doi.org/10.1038/s41563-023-01463-7> (2023).
- Nevius, M. S. et al. Semiconducting graphene from highly ordered substrate interactions. *Phys. Rev. Lett.* **115**, 136802 (2015).
- Conrad, M. et al. Wide band gap semiconductor from a hidden 2D incommensurate graphene phase. *Nano Lett.* **17**, 341–347 (2017).
- N. Nair, M. et al. Band gap opening induced by the structural periodicity in epitaxial graphene buffer layer. *Nano Lett.* **17**, 2681–2689 (2017).
- Kim, S., Ihm, J., Choi, H. J. & Son, Y.-W. Origin of anomalous electronic structures of epitaxial graphene on silicon carbide. *Phys. Rev. Lett.* **100**, <https://doi.org/10.1103/physrevlett.100.176802> (2008).
- Riedl, C., Coletti, C., Iwasaki, T., Zakharov, A. A. & Starke, U. Quasi-free-standing epitaxial graphene on SiC obtained by hydrogen intercalation. *Phys. Review Letters* **103**, <https://doi.org/10.1103/physrevlett.103.246804> (2009).
- Emery, J. D. et al. Structural consequences of hydrogen intercalation of epitaxial graphene on SiC(0001). *Appl. Phys. Lett.* **105**, 161602 (2014).
- Wong, D. et al. Characterization and manipulation of individual defects in insulating hexagonal boron nitride using scanning tunnelling microscopy. *Nat. Nanotechnol.* **10**, 949–953 (2015).
- Lee, J. et al. Imaging electrostatically confined Dirac fermions in graphene quantum dots. *Nat. Phys.* **12**, 1032–1036 (2016).
- Ghahari, F. et al. An on/off Berry phase switch in circular graphene resonators. *Science* **356**, 845–849 (2017).
- Krebs, Z. J. et al. Imaging the breaking of electrostatic dams in graphene for ballistic and viscous fluids. *Science* **379**, 671–676 (2023).
- Lee, D. H. & Gupta, J. A. Tunable field control over the binding energy of single dopants by a charged vacancy in GaAs. *Science* **330**, 1807–1810 (2010).
- Teichmann, K. et al. Controlled charge switching on a single donor with a scanning tunneling microscope. *Phys. Rev. Lett.* **101**, <https://doi.org/10.1103/physrevlett.101.076103> (2008).
- Kitchen, D., Richardella, A., Tang, J.-M., Flatté, M. E. & Yazdani, A. Atom-by-atom substitution of Mn in GaAs and visualization of their hole-mediated interactions. *Nature* **442**, 436–439 (2006).
- Yakunin, A. M. et al. Spatial structure of an individual Mn acceptor in GaAs. *Phys. Rev. Lett.* **92**, <https://doi.org/10.1103/physrevlett.92.216806> (2004).
- Zheng, H., Weismann, A. & Berndt, R. Manipulation of subsurface donors in ZnO. *Phys. Rev. Lett.* **110**, <https://doi.org/10.1103/physrevlett.110.226101> (2013).
- Nguyen, G. D. et al. 3D imaging and manipulation of subsurface selenium vacancies in PdSe₂. *Phys. Rev. Lett.* **121**, 086101 (2018).

60. Wang, C., You, L., Cobden, D. & Wang, J. Towards two-dimensional van der Waals ferroelectrics. *Nat. Mater.* <https://doi.org/10.1038/s41563-022-01422-y> (2023).
61. Han, Y., Evans, J. W. & Tringides, M. C. Dy adsorption on and intercalation under graphene on 6H-SiC(0001) surface from first-principles calculations. *Phys. Rev. Mater.* **5**, 074004 (2021).
62. Kolmer, M. et al. Highly asymmetric graphene layer doping and band structure manipulation in rare earth-graphene heterostructure by targeted bonding of the intercalated gadolinium. *J. Phys. Chem. C.* **126**, 6863–6873 (2022).
63. Varchon, F., Mallet, P., Veuillen, J. Y. & Magaud, L. Ripples in epitaxial graphene on the Si-terminated SiC(0001) surface. *Phys. Rev. B* **77**, <https://doi.org/10.1103/physrevb.77.235412> (2008).
64. Emery, J. D. et al. Chemically Resolved Interface Structure of Epitaxial Graphene on SiC(0001). *Phys. Rev. Lett.* **111**, <https://doi.org/10.1103/physrevlett.111.215501> (2013).
65. Martinez-Castro, J. et al. Electric polarization switching in an atomically thin binary rock salt structure. *Nat. Nanotechnol.* **13**, 19–23 (2018).
66. Hus, S. M. et al. Observation of single-defect memristor in an MoS₂ atomic sheet. *Nat. Nanotechnol.* **16**, 58–62 (2021).
67. Lauffer, P. et al. Atomic and electronic structure of few-layer graphene on SiC(0001) studied with scanning tunneling microscopy and spectroscopy. *Phys. Rev. B* **77**, 155426 (2008).
68. Červenka, J., Van De Ruit, K. & Flipse, C. F. J. Giant inelastic tunneling in epitaxial graphene mediated by localized states. *Phys. Rev. B* **81**, 205403 (2010).
69. Liu, C. & Wang, J. Spectroscopic evidence for electron correlations in epitaxial bilayer graphene with interface-reconstructed superlattice potentials. *Chin. Phys. Lett.* **39**, (2022).
70. Kolmer, M. et al. Breaking of inversion symmetry and interlayer electronic coupling in bilayer graphene heterostructure by structural implementation of high electric displacement fields. *J. Phys. Chem. Lett.* **13**, 11571–11580 (2022).
71. Conrad, M. et al. Structure and evolution of semiconducting buffer graphene grown on SiC(0001). *Phys. Rev. B* **96**, 195304 (2017).
72. Ponomarenko, L. A. et al. Cloning of Dirac fermions in graphene superlattices. *Nature* **497**, 594–597 (2013).
73. Dean, C. R. et al. Hofstadter’s butterfly and the fractal quantum Hall effect in moiré superlattices. *Nature* **497**, 598–602 (2013).
74. Wang, E. et al. Gaps induced by inversion symmetry breaking and second-generation Dirac cones in graphene/hexagonal boron nitride. *Nat. Phys.* **12**, 1111–1115 (2016).
75. Kresse, G. & Furthmüller, J. Efficient iterative schemes for ab initio total-energy calculations using a plane-wave basis set. *Phys. Rev. B* **54**, 11169–11186 (1996).
76. Kresse, G. & Joubert, D. From ultrasoft pseudopotentials to the projector augmented-wave method. *Phys. Rev. B* **59**, 1758–1775 (1999).
77. Klimeš, J., Bowler, D. R. & Michaelides, A. Chemical accuracy for the van der Waals density functional. *J. Phys. Condens. Matter* **22**, 022201 (2010).
78. Li, W. et al. Thickness-dependent energetics for Pb adatoms on low-index Pb nanofilm surfaces: First-principles calculations. *Phys. Rev. B* **96**, 205409 (2017).
79. Momma, K. & Izumi, F. VESTA 3 for three-dimensional visualization of crystal, volumetric and morphology data. *J. Appl. Crystallogr.* **44**, 1272–1276 (2011).
80. Omidian, M. et al. Structural and local electronic properties of clean and Li-intercalated graphene on SiC(0001). *Surf. Sci.* **699**, 121638 (2020).

Acknowledgements

This work was supported by the U.S. Department of Energy (DOE), Office of Science, Basic Energy Sciences, Materials Science and Engineering Division. The research was performed at the Ames National Laboratory, which is operated for the U.S. DOE by Iowa State University under contract # DE-AC02-07CH11358. DFT calculations were performed with a grant of computer time at the National Energy Research Scientific Computing Center (NERSC). NERSC is a DOE Office of Science User Facility supported by the Office of Science of the U. S. DOE under Contract No. DE-AC02-05CH11231. We thank BeeGraphene for collaborating and providing reference samples. We thank James W. Evans for valuable discussions about this project.

Author contributions

M.K. and M.C.T. designed the project and discussed its progress. S.C. and M.K. performed synthesis. J.H. and S.R. under the supervision of M.K. carried out STM experiments. J.H., S.C., Z.F., and M.K. analyzed experimental data. Y.H. performed DFT calculations. M.K. coordinated the work and wrote the manuscript with contributions from all authors. All authors have given approval to the final version of the manuscript.

Competing interests

The authors declare no competing interests.

Additional information

Supplementary information The online version contains supplementary material available at <https://doi.org/10.1038/s42005-023-01515-3>.

Correspondence and requests for materials should be addressed to Marek Kolmer.

Reprints and permission information is available at <http://www.nature.com/reprints>

Publisher’s note Springer Nature remains neutral with regard to jurisdictional claims in published maps and institutional affiliations.



Open Access This article is licensed under a Creative Commons Attribution 4.0 International License, which permits use, sharing, adaptation, distribution and reproduction in any medium or format, as long as you give appropriate credit to the original author(s) and the source, provide a link to the Creative Commons license, and indicate if changes were made. The images or other third party material in this article are included in the article’s Creative Commons license, unless indicated otherwise in a credit line to the material. If material is not included in the article’s Creative Commons license and your intended use is not permitted by statutory regulation or exceeds the permitted use, you will need to obtain permission directly from the copyright holder. To view a copy of this license, visit <http://creativecommons.org/licenses/by/4.0/>.

© The Author(s) 2024